

A computational method of pressure drop loss of cross-wavy primary surface recuperator for SOFC-MGT

Chong Qiu¹, Yanzhao Yang^{1*}, Fu Chen², Jianyang Yu², Yanping Song²

¹ School of Mechanical and Electrical Engineering, TaiZhou University, Jiangsu, 225300, China,

*E-mail: 626462128@qq.com;

² School of Energy Science and Engineering, Harbin Institute of Technology, Heilongjiang 150006, China,

E-mail: chenfu@hit.edu.cn

Abstract: The rapid development of SOFC-MGT system, as an important component of decarbonization in the aviation industry, has led to the annular cross-wavy primary surface recuperator (CWPSR) becoming a key area of research for many scientists due to its high efficiency, lightweight, and high compactness. However, accurately calculating pressure drop loss is difficult due to the complex curved channels, wall interfaces, and airflow direction. In this work, a mathematical model was developed for the heat exchange cell of the annular cross-wavy primary surface recuperator based on segmented air and gas channels. In order to facilitate engineering applications, this study has been summarized the distribution of pressure loss coefficient with Reynolds number for each part through three-dimensional numerical simulation technology. The results were validated using a fluid-solid heat coupling numerical model and test data, showing good consistency between the computational method and the numerical simulation. The maximum deviations between calculation results and numerical simulation data for the air channel were 10.425%, 10.354%, and 10.954% for inclination angles of $\alpha=30^\circ$, 45° , and 60° , respectively. For the gas channel, the maximum deviation was 7.151%.

Keywords: SOFC-MGT, Annular CWPSR, Heat exchange cell, Pressure drop loss, Computational method.

NOMENCLATURE:

Symbols			
a	Long side of trapezoid of inlet and outlet structure (mm)	ρ	Density (kg/m ³)
A_i	Cross-sectional area (mm ²)	μ	Dynamic viscosity of the fluid (Pa·s)
A_w	Heat transfer area (mm ²)	λ_f	Thermal conductivity of fluid (W/m ² /K)
b	CW channel length (mm)	ξ	Pressure drop loss coefficient
c	Channel radial height for heat exchange core (mm)	U_{av}	Average velocity in the vertical section direction (m/s)
d	Long side of trapezoid of air inlet structure (mm)	ΔP	Pressure difference (Pa)
D_e	Equivalent diameter of CW channel (mm)	ΔT	Logarithmic man temperature difference for the gas and air (K)
f	Fanning friction factor	Subscripts	
h	Heat transfer coefficient (mm)	a	Air
l	Channel length of air inlet structure	a-in	Inlet of air

L	Channel length of CW channel (mm)	a-out	Outlet of air
Nu	Nusselt number	g	Gas
q_m	Mass flow rate of each CW channel	i	Each CW channel
Q	Heat transfer rate (W)	w	Wall
Q_1	Absorbed heat of endothermic process 2-4 (W)	w-in	Wall at CW channel inlet
Q_2	Released heat of endothermic process 5-1 (W)	w-out	Wall at CW channel outlet
Re	Reynolds number	Acronyms	
Greek letters		SOFC-MGT	Solid oxide fuel cell combined with micro gas turbine
α	Inclination angle of the inlet and outlet structure (deg)	CWPSR	Cross-wavy primary surface recuperator
β	$90^\circ - \alpha$ (deg)	CW	Cross-wavy
		HEC	Heat exchange cell

1 INTRODUCTION

Currently, carbon dioxide emissions from the aviation industry contribute to more than 2% of the global total [1]. It is concerning that these emissions are growing at an annual rate of 3.6% [2]. If this trend persists, carbon dioxide emissions from the aviation industry could increase by 2.4 to 3.6 times by 2050 compared to the current levels [3]. During that period, carbon dioxide emissions from the aviation industry could become a primary driver of global climate and environmental change. Therefore, aviation decarbonization has become an urgent task for sustainable development in the aviation industry. Given this context, there is growing interest in low-carbon, efficient, high-energy-density solid oxide fuel cell combined with micro gas turbine (SOFC-MGT) technology for power generation [4-6]. This technology holds the potential to be a key solution for decarbonizing aviation. Solid oxide fuel cells can directly convert the chemical energy of fuel into electrical energy, and micro gas turbines can further convert the high-temperature and high-pressure exhaust gas of solid oxide fuel cells into electrical energy [7-9]. Its overall efficiency can exceed 70%, surpassing the efficiency of traditional aviation engines. In addition, compared to other traditional batteries, solid-state oxide fuel cells have a higher energy density [10, 11]. This means that solid oxide fuel cell can not only solve the problem of aviation decarbonization, but also meet the demand for long-term endurance.

As shown in Fig. 1, SOFC-MGT is divided into series and parallel systems based on whether secondary fuel is added to the combustion chamber [12-14]. In a series system, as shown in Fig. 1(a), the gas from the combustion chamber outlet first heats the cathode air and then enters the turbine for work. Moreover, the combustion chamber is filled with a mixture of partially reacted gases from the SOFC exhaust. In a parallel system (Fig. 1(b)), additional fuel in the combustion chamber raises the gas temperature at the outlet compared to the series system. Therefore, high-temperature gas first enters the turbine of the micro gas turbine to expand and work, and then the residual temperature at the turbine outlet is used to heat the cathode air.

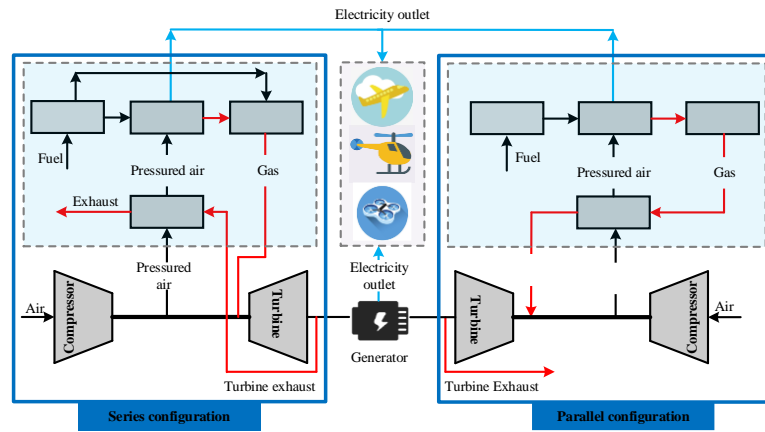


Fig. 1 Configuration diagram of aviation SOFC-MGT hybrid system [12-14]

In the SOFC-MGT system, the heat exchanger is one of the crucial components. There are significant differences between heat exchangers used in aviation power systems and those used in ground equipment. In addition to considering heat transfer and flow resistance characteristics, lightweight and high compactness should also be considered [15-17]. This is because lighter and smaller heat exchangers typically result in higher load capacity and extended endurance in aviation power systems. The cross-wavy primary surface recuperator (CWPSR) has emerged as an ideal choice for SOFC-MGT systems intended for aviation power applications, owing to its high efficiency, lightweight, and compact design [18]. However, the high compactness characteristic requires the channel size to be only in millimeters, resulting in the boundary layer penetrating the entire channel cross-section. To mitigate the impact of the boundary layer, enhance secondary flow, and improve the heat transfer performance of the heat exchanger, the channel is designed with a CW-shaped corrugated structure [19]. However, this design results in a deterioration of the flow resistance characteristics of the heat exchanger, leading to increased compressor power consumption and turbine back pressure, consequently reducing the overall efficiency of the SOFC-MGT system. In addition, one of the key technical challenges for SOFC-MGT applied in the field of aviation power is how to effectively reduce its flow resistance characteristics while maintaining the lightweight, highly compact, and efficient characteristics of the heat exchanger [20-23]. This requires comprehensive consideration of the structural design, fluid dynamics, and heat transfer of the heat exchanger to ensure optimal performance of the system in aviation applications. The CWPSR is a highly desirable option for SOFC-MGT due to its compact structure, high heat exchange efficiency, low pressure loss, light weight, and high reliability [24, 25]. This type of recuperator has been successfully applied to various MGT models, such as the C30, C65, and C200 from Capstone Corporation (as shown in Fig. 2) [24].



Fig. 2 CWPSR applied on Capstone C30 [24]

Currently, research is underway to investigate the heat transfer and flow resistance characteristics of the CW-type original surface heat exchanger. Utriainen and Sundén [26] discussed the trend towards compact

regenerators in MGT and proposed a numerical simulation model of the simplified cross-wavy channel (SCC). They later constructed a numerical model of the CW channel based on the N-S equation and periodic boundary conditions, which allowed for detailed analysis of flow and heat transfer characteristics, as well as pressure drop loss, using three-dimensional numerical simulation technology [27]. To explore the potential of different types of regenerators, Utriainen and Sundén [28] compared four different heat exchange surfaces used in a 50 kW micro gas turbine, using the volume goodness factor and flow area goodness factor. Their results indicated that the CW2-z3 surface had smaller volume and the CC-75 surface had smaller weight, with the primary reason being the higher compactness of the CW primary surface regenerator. Consequently, the CWPSR has more potential for use in portable mobile power supply compared to the other three heat exchange surfaces. Various studies have since been conducted to investigate the heat transfer characteristics and pressure loss of CWPSR under different working conditions. Wang et al. [29] developed the CWPSR for a 100 kW micro gas turbine and measured the relationship between the total heat transfer coefficient and pressure loss using a whole machine test with Reynolds numbers ranging from 250 to 400. Liang et al. [30] developed a CWPSR suitable for a 100 kW micro gas turbine and analyzed the effects of mass flow rate, gas inlet temperature, and air inlet pressure on its heat transfer characteristics and pressure loss, proposing empirical formulas under different working conditions.

Further studies investigated the thermodynamic characteristics of CW type channels, including the effects of the amplitude to channel pitch (A/P) on heat transfer and pressure drop. Empirical relationships for the Nusselt number and friction factor were obtained for CWPSR under variable flow conditions using whole machine test data [31, 32]. Nanofluid flow and heat transfer characteristics were analyzed in wavy channels with numerical simulation, and the distribution of heat transfer characteristics along the CW channel was established by experiment [33, 34]. Design and optimization methods were also proposed for annular CWPSR based on component of pressure loss and entropy generation performance, respectively. Cai et al. [35] used genetic algorithm to solve the optimization problem of annular CWPSR and verified the method with test data from regenerators applied with the C30 and C65. Shi et al. [36] researched the influence of main structural parameters on the irreversible loss of the CW channel using fluid-solid coupled heat transfer of SCC at Reynolds number of $Re=100-1300$. Finally, Li et al. [37] proposed a design method for an annular CWPSR used in portable microturbine generators and verified it through whole machine test.

In summary, the research pertaining to CWPSR has predominantly concentrated on the heat transfer and flow resistance characteristics, leading to the formulation of empirical equations based on these attributes. However, these empirical equations face challenges in their universal applicability to heat exchangers with diverse structural configurations, and their guidance for the early-stage investigation of CWPSR remains ambiguous. This paper introduces an estimation methodology for pressure drop losses, tailored to different structural variations. This approach enables the initial estimation of pressure drop losses in CWPSR, accounting for varying structural types.

This study divided the air and gas channels of the heat exchange core for the CWPSR into seven parts based on pressure drop loss types. The pressure drop loss equation for each part was constructed using the empirical formula for pressure drop loss in pipelines. The distribution of pressure drop loss coefficients of each part with Reynolds number has been summarized with three-dimensional numerical simulation technology. In future engineering applications, the pressure drop loss coefficient can be directly calculated based on this distribution

characteristic, without further numerical simulation. Finally, the total pressure loss of the heat exchange core was determined by summing the pressure losses of each part. As a result, this study obtained the pressure drop loss equation and corresponding coefficient value range for the heat exchange core, providing a computational method for calculating pressure drop loss in engineering applications. This method reduces the need for direct numerical simulation and testing of the heat exchange core, thus decreasing the design cycle and cost.

2 Mathematical model

2.1 Physical model

Fig. 3 depicts the structure of the heat exchange core (HEC) and the pressure drop loss components for the annular CWPSR installed on the micro gas turbine. The HEC consists of six main parts: the air inlet structure, air CW channel structure, air outlet structure, gas inlet structure, gas CW channel structure, and gas outlet structure. The pressure drop loss components for the air and gas channels are described as follows.

Component of pressure drop loss for air channel:

a) Local pressure drop loss at the air inlet ($\Delta P_{a(1-2)}$). This pressure drop loss is mainly caused by the sudden shrink of channel cross-section and the change of airflow direction.

b) Pressure drop loss along the channel of air inlet structure ($\Delta P_{a(2-3)}$). This pressure drop loss is mainly caused by the viscous friction between fluid and solid wall.

c) Local pressure drop loss at the interface between air inlet structure and CW channel structure ($\Delta P_{a(3-4)}$). This pressure drop loss is mainly composed of two parts. One is that the shape of the channel section of the air inlet structure is different from that of the CW channel structure, resulting in the existence of wall at the interface. The other is that the inlet structure forces the airflow into the CW channel at included angle of β , resulting in the diversion of the airflow direction.

d) Pressure drop loss along air CW channel ($\Delta P_{a(4-5)}$). Since the CW channel is composed of complex curved surfaces, in addition to the pressure drop loss caused by viscous friction, there is also the reduction of mechanical energy caused by vortex in the channel.

e) Local pressure drop loss at the interface between air CW channel structure and outlet structure ($\Delta P_{a(5-6)}$). This physical model is the same as that of $\Delta P_{a(3-4)}$, but the airflow direction is opposite.

f) Pressure drop loss along the channel of air outlet structure ($\Delta P_{a(6-7)}$). This physical model is the same as that of $\Delta P_{a(2-3)}$, but the airflow direction is opposite.

g) Local pressure drop loss at the air outlet ($\Delta P_{a(7-8)}$). This pressure drop loss is mainly caused by the sudden expansion of channel cross-section and the change of airflow direction.

Component of pressure drop loss for gas channel:

a) Local pressure drop loss at the gas inlet ($\Delta P_{g(1-2)}$). This pressure drop loss is mainly caused by the sudden shrink of channel cross-section.

b) Pressure drop loss along the channel of gas inlet structure ($\Delta P_{g(2-3)}$). This pressure drop loss is mainly caused by the viscous friction between fluid and solid wall.

c) Local pressure drop loss at the interface between air inlet structure and CW channel structure ($\Delta P_{g(3-4)}$). This pressure drop loss is caused by the different section shapes between the gas inlet structure channel and the gas CW channel.

d) Pressure drop loss along gas CW channel ($\Delta P_{g(4-5)}$). The cause of pressure drop loss here is similar to that of $\Delta P_{g(4-5)}$ on the air side.

- e) Local pressure drop loss at the interface between gas CW channel structure and outlet structure ($\Delta P_{g(5-6)}$). This physical model is the same as that of $\Delta P_{g(3-4)}$, but the airflow direction is opposite.
- f) Pressure drop loss along the channel of gas outlet structure ($\Delta P_{g(6-7)}$). This physical model is the same as that of $\Delta P_{g(2-3)}$, but the airflow direction is opposite.
- g) Local pressure drop loss at the gas outlet ($\Delta P_{g(7-8)}$). This pressure drop loss is mainly caused by the sudden expansion of channel cross-section.

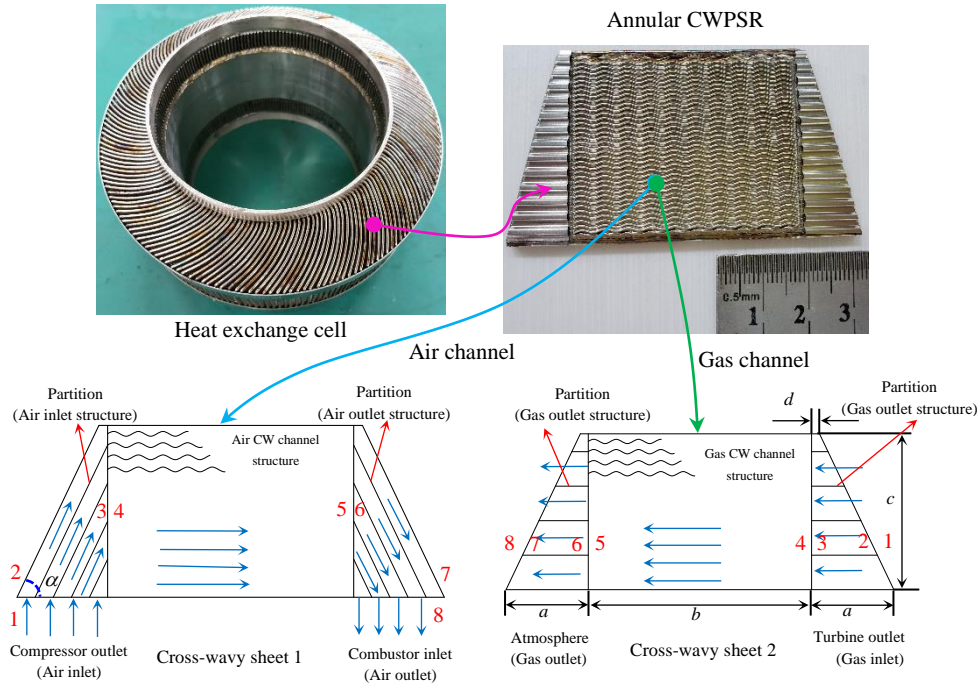


Fig. 3 Geometric sketch and component of pressure losses of HEC for annular CWPSR

Fig. 3 illustrates the connection of the air channel inlet for the annular CWPSR with the outlet of the centrifugal compressor, and the outlet of the air channel with the inlet of the combustion chamber. The annular CWPSR is employed to absorb heat from the high-temperature exhaust discharged from the radial flow turbine into high-pressure air with a certain temperature, thereby converting low-temperature and high-pressure air at the compressor outlet into high-temperature and high-pressure air, and saving the fuel consumption of the micro gas turbine.

2.2 Computational model of heat transfer and pressure drop

The annular CWPSR primarily undergoes heat exchange in the CW channel. As a result, the study of the regenerator's heat transfer and flow resistance characteristics is based on the Reynolds number in the CW channel. The Reynolds number (Re) can be written as:

$$\text{Re} = \frac{\rho \cdot U_{av} \cdot D_e}{\mu} \quad (2-1)$$

where U_{av} , μ , ρ and D_e are the average velocity in the CW channel section, the dynamic viscosity, density and hydraulic diameter, respectively. Based on Reynolds number, the mass flow rate of each CW channel is defined as:

$$q_m = \frac{\text{Re} \cdot \mu \cdot A_i}{D_e} \quad (2-2)$$

where A_i is the area of each CW channel. The Nusselt number (Nu) representing the heat exchange capacity

of the HEC is calculated by:

$$Nu = \frac{h_w \cdot D_e}{\lambda_f} \quad (2-3)$$

where h_w and λ_f is the heat transfer coefficient and thermal conductivity.

Fig. 4 illustrates the heat transfer process between high-temperature gas and low-temperature air, which occurs through the wall as the medium. This process can be broken down into three steps. First, convective heat transfer occurs between the high-temperature gas and the wall, resulting in the transfer of heat from the high-temperature gas to the low-temperature wall. Next, the heat flows from the high-temperature side of the wall to the low-temperature side. Finally, the low-temperature air absorbs heat from the high-temperature wall through convective heat transfer.

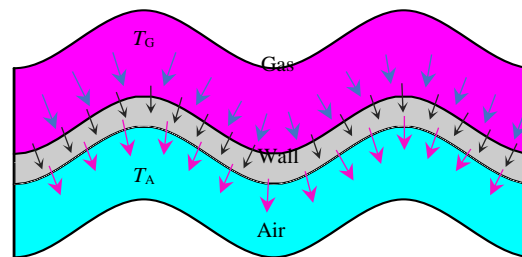


Fig. 4 Heat transfer model between gas and air channel

The heat transfer coefficient h_w between air and wall is calculated as follows:

$$h_w = \frac{Q_w}{\Delta T_w \cdot A_w} \quad (2-4)$$

where Q_w , h_w , and A_w are the heat transfer rate, heat transfer coefficient, and heat exchange area, respectively. T_w is the logarithmic mean temperature difference for the air and wall, which can be obtained by Eq. (2-6) [33]:

$$\Delta T_w = \frac{(T_{a-in} - T_{w-in}) - (T_{a-out} - T_{w-out})}{\ln[(T_{a-in} - T_{w-in}) / (T_{a-out} - T_{w-out})]} \quad (2-5)$$

As shown in Fig. 5, T_{a-in} and T_{a-out} are the mass flow average temperature in the inlet and outlet sections. T_{w-in} and T_{w-out} refer to the wall temperature of the inlet and outlet, respectively.

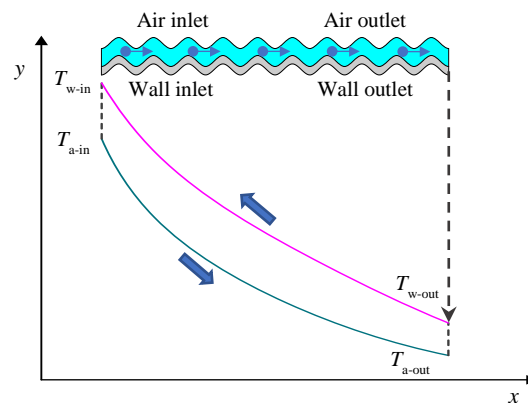


Fig. 5 Schematic diagram of temperature distribution along CW channel

The Fanning friction coefficient f_{air} is usually used to express the characteristics of fluid pressure loss [35, 37, 38]:

$$f_{\text{air}} = \frac{\Delta P \cdot D_e}{0.5 \rho \cdot L \cdot U_{av}^2} \quad (2-6)$$

where L is the channel length of CW channel.

3 Computational method of pressure drop losses for heat exchange core

To determine the pressure drop loss in the air and gas channels, empirical formulas for pressure drop loss in pipelines can be used to derive four local pressure drop loss equations and three pressure drop loss equations along the channel. However, each equation contains unknown coefficients. In this study, ANSYS CFX2021 R1, a commercial software, is utilized to calculate the actual pressure drop and fluid physical properties of each component, enabling the determination of the coefficients in each equation. The following chapters will provide a detailed explanation of the methodology used to calculate the pressure drop loss coefficients for different sections of the heat exchange core.

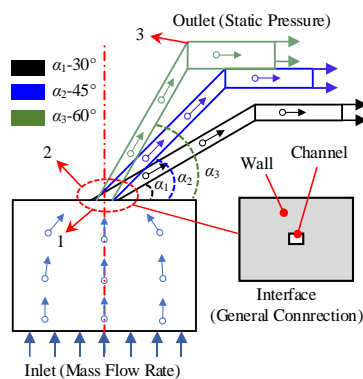
3.1 Computational method of pressure drop losses for air channel

3.1.1 Pressure drop losses for 1-2

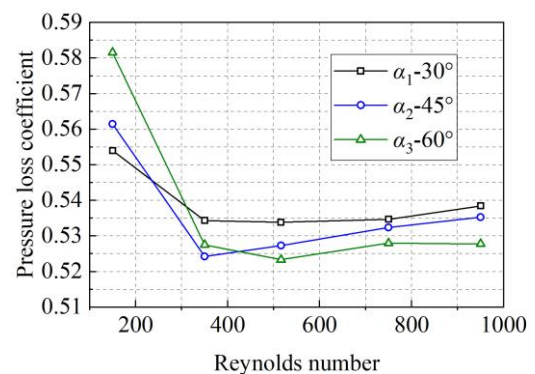
Fig. 6 illustrates the physical model and local pressure drop loss coefficient of the air channel inlet at inclination angles of $\alpha=30^\circ$, 45° , and 60° . In Fig. 7(a), the green, blue, and black lines represent the numerical model of the air channel inlet with the angles $\alpha_1=60^\circ$, $\alpha_2=45^\circ$, and $\alpha_3=30^\circ$, respectively. The inlet and outlet boundary conditions for 1-2 are set as total pressure and mass flow, respectively. The total pressure at the heat exchange core's inlet is the same as the outlet pressure of the compressor (239735 Pa), while the mass flow at the outlet is calculated based on the Reynolds number and hydraulic diameter of channel 2-3. The local pressure loss at the air channel inlet is due to the sudden reduction of the channel section and the inclination angle α . By applying the empirical formula (3-1) for local pressure drop loss, the pressure drop loss coefficient distribution (shown in Fig. 7(b)) is obtained through three-dimensional numerical simulation. The pressure drop loss coefficient $\xi_{a(1-2)}$ decreases gradually with increasing Reynolds number for all three inclination angles. At low Reynolds numbers, the pressure drop loss at $\alpha_3=30^\circ$ is lower than that at $\alpha_2=45^\circ$ and $\alpha_3=60^\circ$, whereas at high Reynolds numbers, the pressure drop loss at $\alpha_3=60^\circ$ is lower.

$$\Delta p_{a(1-2)} = \xi_{a(1-2)} \frac{\rho_{a(1-2)} \bar{u}_{a2}^2}{2} \quad (3-1)$$

where $\Delta p_{a(1-2)}$, $\rho_{a(1-2)}$, and \bar{u}_{a2}^2 are the pressure drop on both sides of the interface 1, density at air channel inlet, and average velocity at the section 2, respectively.



(a) Physical model



(b) Pressure drop loss coefficient $\xi_{a(1-2)}$

Fig. 6. Local pressure drop loss coefficient at air channel inlet with inclination angle of $\alpha=30^\circ$, 45° , and 60°

3.1.2 Pressure drop losses for 2-3 and 6-8

Fig. 7 describes the pressure drop loss coefficient across the channels of the air inlet and outlet structure at inclination angles of $\alpha=30^\circ$, 45° , and 60° . The pressure drop loss is computed for positions 2-3 and 6-8 using the numerical model and boundary conditions presented in Fig. 6 (a). As shown in Fig. 7 (a), the length of each channel in the air inlet structure varies, leading to differing pressure drop losses in each channel. However, the pressure drop loss model remains the same, allowing the pressure drop loss coefficient for different channels to be set to a constant value. Thus, any channel can be selected as the research subject when investigating the pressure drop loss coefficient. The distribution of the pressure drop loss coefficient $\lambda_{a,i(2-3)}$ for the air inlet and outlet structure's channel is shown in Fig. 7 (b), in accordance with the empirical formula (3-3) of pressure drop loss across the channels. For the inclination angles of $\alpha=30^\circ$, 45° , and 60° , the pressure drop loss coefficient across the channels decreases with increasing Reynolds number. Moreover, as the inclination angle α increases, the pressure drop loss coefficient along the channels also decreases.

$$l_{a,i} = \frac{c_{a,i}}{\sin \alpha} \quad (3-2)$$

$$\Delta p_{a,i(2-3)} = \lambda_{a,i(2-3)} \frac{c_{a,i}}{D_{ae,i(2-3)} \sin \alpha} \frac{\rho_{a,i(2-3)} \bar{u}_{a,i(2-3)}^2}{2} \quad (3-3)$$

where $l_{a,i}$, $c_{a,i}$, $\Delta p_{a,i(2-3)}$, $D_{ae,i(2-3)}$, $\rho_{a,i(2-3)}$, and $\bar{u}_{a,i(2-3)}$ are the channel length, the channel radial height, the pressure drop between inlet and outlet for channel 2-3, the hydraulic diameter of channel 2-3, the average value of density in the channel 2-3, and the average value of velocity in the channel 2-3, respectively.

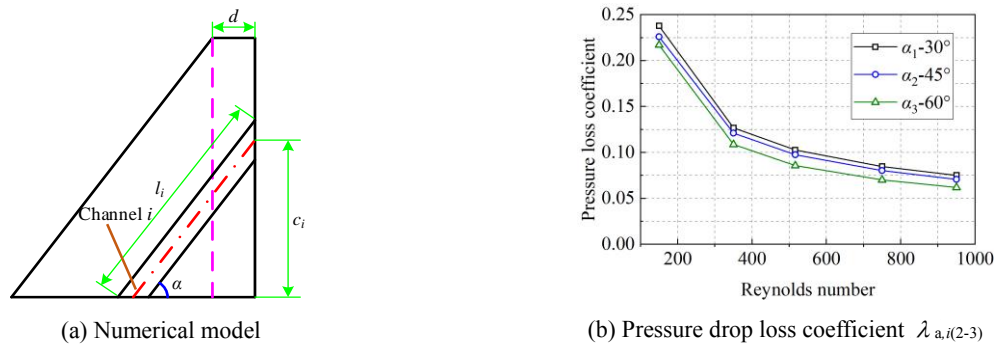


Fig. 7 Pressure drop loss coefficient along channels for air inlet and outlet structure with inclination angle of $\alpha=30^\circ$, 45° , and 60°

3.1.3 Pressure drop losses for 3-4

Fig. 8 shows the local pressure drop loss coefficient at the air CW channel inlet with angles of inclination $\alpha=30^\circ$, 45° , and 60° . The physical model of the inlet is shown in Fig. 8(a) using green, blue, and black structures with included angles of $\beta_1=60^\circ$ ($\beta_1=90^\circ - \alpha_1$), $\beta_2=45^\circ$ ($\beta_2=90^\circ - \alpha_2$), and $\beta_3=30^\circ$ ($\beta_3=90^\circ - \alpha_3$), respectively. The inlet and outlet boundary conditions for 3-4 are set as total pressure and mass flow, respectively. The total pressure at the heat exchange core's inlet is from section 3. The wall boundary conditions for the extension section are no slip wall, and thus, the pressure drop loss along the extension section is neglected. The outlet's mass flow is computed based on the Reynolds number and hydraulic diameter at section 4. As the cross-sectional shape of the air inlet structure channel differs from that of the CW channel, a wall exists at the interface 2 between them, and the orifice model defines this pressure drop loss. The local pressure drop loss coefficient $\xi_{a(3-4)}$ at the air CW channel inlet decreases gradually with the Reynolds number increase. Moreover, with the

α inclination angle increase, the local pressure loss coefficient decreases significantly. At the air CW channel inlet decreases gradually with the Reynolds number increase. Moreover, with the α inclination angle increase, the local pressure loss coefficient decreases significantly. At the included angle of $\beta_3=30^\circ$, the local pressure loss coefficient initially increases and then decreases, but this trend vanishes with the increase of inclination angle α .

$$\Delta p_{a(3-4)} = \xi_{a(3-4)} \frac{\rho_{a(3-4)} \bar{u}_{a4}^2}{2} \quad (3-4)$$

where $\Delta p_{a(3-4)}$, $\rho_{a(3-4)}$, and \bar{u}_{a4}^2 are defined as the pressure drop on both sides of the interface 2, the density at the CW channel inlet, and the average velocity of CW channel section, respectively.

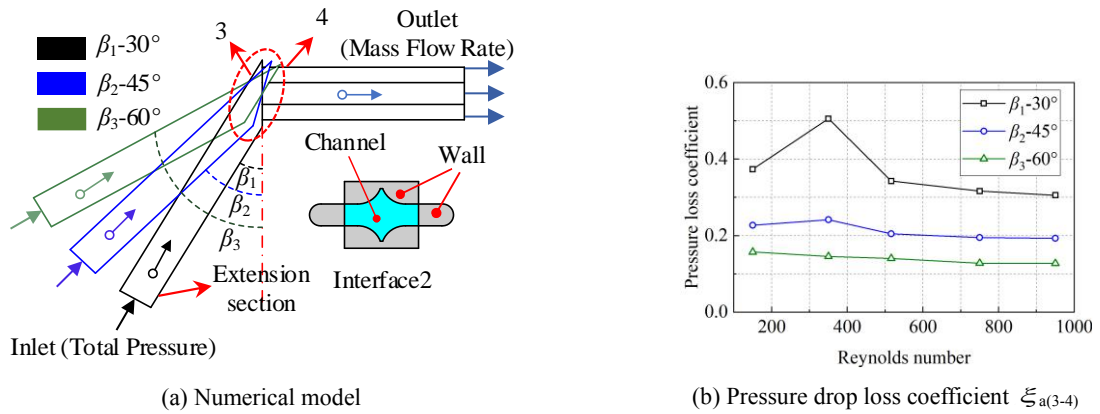


Fig. 8 Local pressure drop loss coefficient at inlet of air CW channel with inclination angle of $\alpha=30^\circ$, 45° , and 60°

3.1.4 Pressure drop losses for 4-5

Fig. 9 presents the pressure drop loss coefficient along the air CW channel with the inclination angles of $\alpha=30^\circ$, 45° , and 60° . The boundary conditions for 4-5 specify the total pressure and mass flow at the inlet and outlet, respectively. The inlet total pressure corresponds to the pressure at section 4. The extension section has no-slip wall boundary conditions, leading to the exclusion of pressure drop loss along this section. The outlet mass flow is calculated based on the CW channel. As shown in Fig. 9(a), the CW channel exhibits corrugations in the main flow direction, resulting in a periodic variation of its cross-section due to the half-cycle difference between the starting angles of the fluctuation curves for the upper and lower parts. Besides the pressure drop loss resulting from viscous friction, there is also a reduction in mechanical energy due to the vortex in the channel. Fig. 9(b) shows the pressure drop loss coefficient $\lambda_{a,i(4-5)}$ the air CW channel, based on empirical formula (3-5) for various included angles, such as $\beta_1=60^\circ$, $\beta_2=45^\circ$, and $\beta_3=30^\circ$, and Reynolds numbers of 150, 350, 516, and 750. The results indicate a higher pressure drop loss coefficient at $Re=150$ compared to that of $Re=350$, 516, and 750, for β angles of 30° , 45° , and 60° . Moreover, the pressure drop loss coefficient tends to be constant when $Re>350$. The maximum pressure drop loss coefficient occurs at $\beta_3=30^\circ$, and the minimum at $\beta_1=60^\circ$.

$$\Delta p_{a,i(4-5)} = \lambda_{a,i(4-5)} \frac{l_{a,cw,i}}{D_{ae,i(4-5)}} \frac{\bar{\rho}_{a(4-5)} \bar{u}_{a(4-5)}^2}{2} \quad (3-5)$$

where $\Delta p_{a,i(4-5)}$, $l_{a,cw,i}$, $D_{ae,i(4-5)}$, $\rho_{a,i(4-5)}$, and $\bar{u}_{a(4-5)}^2$ are the pressure drop between inlet and outlet for CW channel (4-5), the CW channel length, the hydraulic diameter of channel (4-5), the average value of density in the CW channel (4-5), and the average value of velocity in the CW channel (4-5).

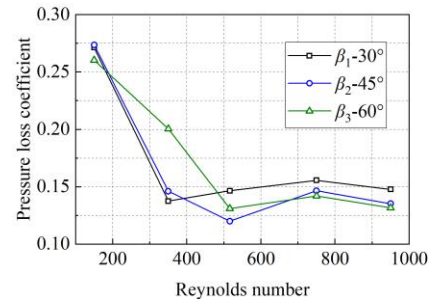
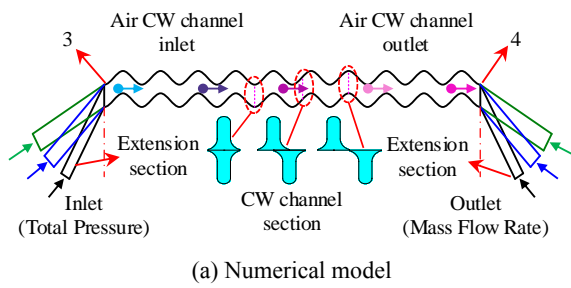


Fig. 9 Pressure drop loss coefficient along air CW channel with inclination angle of $\alpha=30^\circ$, 45° , and 60°

3.1.5 Pressure drop losses for 5-6

As shown in Fig. 10, the local pressure drop loss coefficient at the outlet of air CW channel is investigated for the included angles of $\beta_1=60^\circ$, $\beta_2=45^\circ$, and $\beta_3=30^\circ$. The boundary conditions for sections 5-6 are set as total pressure and mass flow at the inlet and outlet, respectively. The total pressure at the inlet of the heat exchange core is the total pressure at section 5. The boundary conditions for the extension section are set as a no-slip wall, resulting in the pressure drop loss along the extension section being ignored. The mass flow at the outlet is calculated based on the CW channel. As shown in Fig. 10(b), the physical model of the air CW channel outlet is identical to the inlet model, except for the opposite airflow direction. Therefore, the local pressure drop loss model employed at this location is the orifice loss model, and the empirical formula (3-6) for the local pressure drop loss model is provided. The results indicate that, for the included angles of $\beta_1=60^\circ$, $\beta_2=45^\circ$, and $\beta_3=30^\circ$, the local pressure loss coefficient $\xi_{a(5-6)}$ at the outlet of air CW channel decreases slowly with increasing Reynolds number and tends to become constant. Additionally, the included angle α significantly affects the local pressure drop loss coefficient at the outlet of the air CW channel, with this effect decreasing as the inclination angle α increases.

$$\Delta p_{a(5-6)} = \xi_{a(5-6)} \frac{\bar{\rho}_{a(5-6)} \bar{u}_{a6}^2}{2} \quad (3-6)$$

where $\Delta p_{a(5-6)}$, $\rho_{a(5-6)}$, and \bar{u}_{a6}^2 are defined as the pressure drop on both sides of the interface 3, the density at the CW channel outlet, and the average velocity of channel at the air outlet structure, respectively.

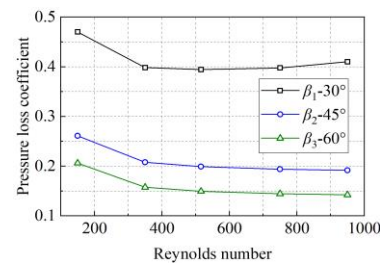
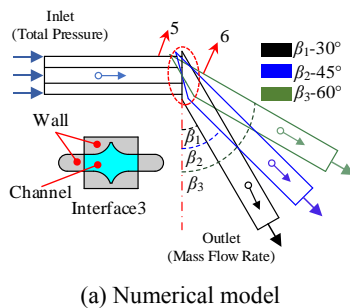


Fig. 10 Local pressure drop loss coefficient at outlet of air CW channel with inclination angle of $\alpha=30^\circ$, 45° , and 60°

3.1.6 Pressure drop losses for 7-8

Fig 11 depicts the physical model of the local pressure drop loss at the outlet of the air channel, which is the same as that at its inlet. The flow direction is opposite, resulting in a sudden expansion of the cross-sectional

area of the channel. The boundary condition is similar to that of position 1-2, and the mass flow is calculated using the Reynolds number and hydraulic diameter at position 6-7. The empirical formula for the local pressure drop loss of sudden expansion for the cross-sectional area is expressed as (3-7). Furthermore, Fig. 11(b) presents the local pressure drop loss coefficient distribution at the outlet of the air channel obtained through three-dimensional numerical simulation. For the inclination angles of $\alpha=30^\circ$, 45° , the local pressure loss coefficient $\xi_{a(7-8)}$ increases gradually with the increase of Reynolds number. However, for the inclination angle of $\alpha=60^\circ$, the local pressure drop loss coefficient first decreases and then increases. It is noteworthy that the local pressure drop loss exhibits an opposite trend with the inclination angle α .

$$\Delta p_{a(7-8)} = \xi_{a(7-8)} \frac{\rho_{a(7-8)} \bar{u}_{a8}^2}{2} \quad (3-7)$$

where $\Delta p_{a(7-8)}$, $\rho_{a(7-8)}$, and \bar{u}_{a8}^2 are the pressure drop on both sides of the interface 4, density at air channel outlet, and velocity at the section 8, respectively.

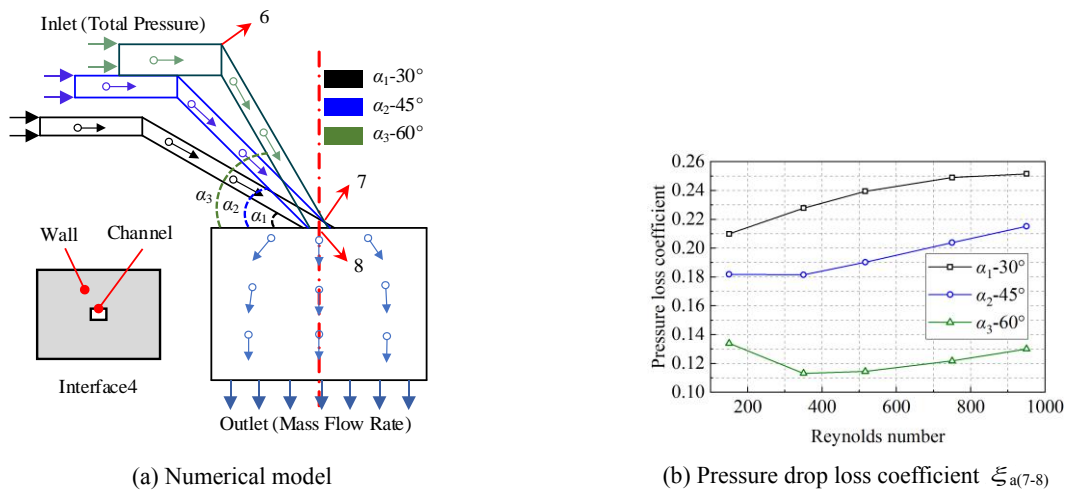


Fig. 11 Local pressure drop loss coefficient at air channel outlet with inclination angle of $\alpha=30^\circ$, 45° , and 60°

3.2 Computational method of pressure drop losses for gas channel

The type of pressure drop loss at each position of the gas channel is similar to that of the air channel, except that the physical properties of the fluid are different. Furthermore, the boundary condition setting method in the gas channel is the same as that in the air channel.

3.2.1 Pressure drop losses for 1-2

Fig. 12 demonstrates that the channel of gas inlet structure, unlike the air inlet structure channel, lacks an inclination angle, resulting in a standard sudden shrink structure and lower local pressure drop loss. The empirical formula (3-8) can be used to express the local pressure drop loss at the inlet of the gas channel. In Fig. 12(b), the local pressure drop loss coefficient $\xi_{g(1-2)}$ at the inlet of the gas channel gradually decreases and reaches a constant value with the increase of Reynolds number.

$$\Delta p_{g(1-2)} = \xi_{g(1-2)} \frac{\rho_{g(1-2)} \bar{u}_{g2}^2}{2} \quad (3-8)$$

where $\Delta p_{g(1-2)}$, $\rho_{g(1-2)}$, and \bar{u}_{g2}^2 are the pressure drop on both sides of the interface 5, density at air channel inlet, and velocity at the section 2, respectively.

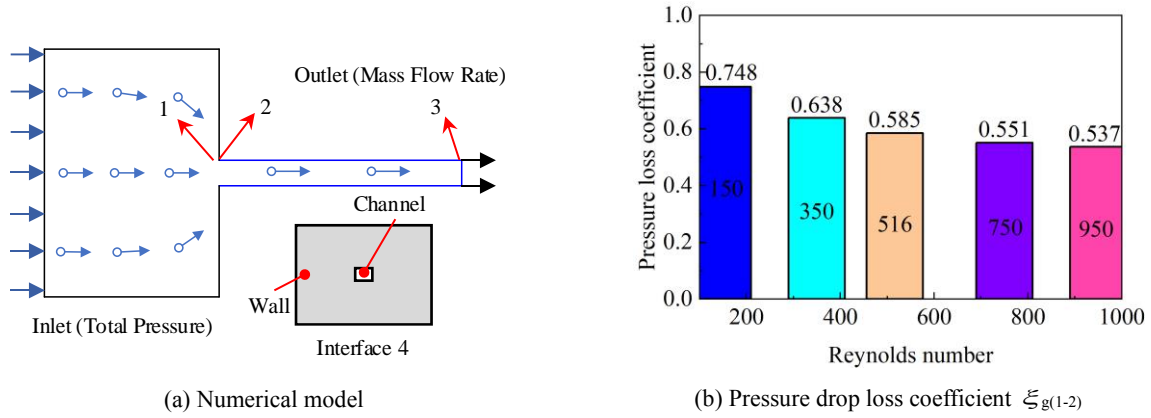


Fig. 12 Local pressure drop loss coefficient at gas channel inlet

3.2.2 Pressure drop losses for 2-3 and 6-8

As depicted in Fig. 13, the trapezoidal shape of the air inlet and outlet structures, due to the inclination angle, results in varying channel lengths for the gas inlet structure. Despite this difference, the pressure drop loss model remains the same for each channel. Therefore, a single channel, with a length of $l_{g,i}$ will be selected for further study. Similar to the loss along channel for the air inlet structure, the loss along channel for the gas inlet structure can be expressed using the empirical formula (3-10). In Fig. 13(b), with the increase of Reynolds number, the pressure drop loss coefficient $\lambda_{g,i(2-3)}$ along channel for the gas inlet and outlet structure decreases gradually.

$$l_{g,i} = d + (c - c_{g,i}) \cot \alpha \quad (3-9)$$

$$\Delta p_{g,i(2-3)} = \lambda_{g,i(2-3)} \frac{d + (c - c_{g,i}) \cot \alpha}{D_{ge,i(2-3)}} \frac{\rho_{g,i(2-3)} \bar{u}_{g,i(2-3)}^2}{2} \quad (3-10)$$

where $c_{g,i}$, $\Delta p_{g,i(2-3)}$, $D_{ge,i(2-3)}$, $\bar{\rho}_{g,i(2-3)}$, and $\bar{u}_{g,i(2-3)}$ are the channel radial height, the pressure drop between inlet and outlet for channel (2-3), the hydraulic diameter of channel (2-3), the average value of density in the channel (2-3), and the average value of velocity in the channel (2-3), respectively.

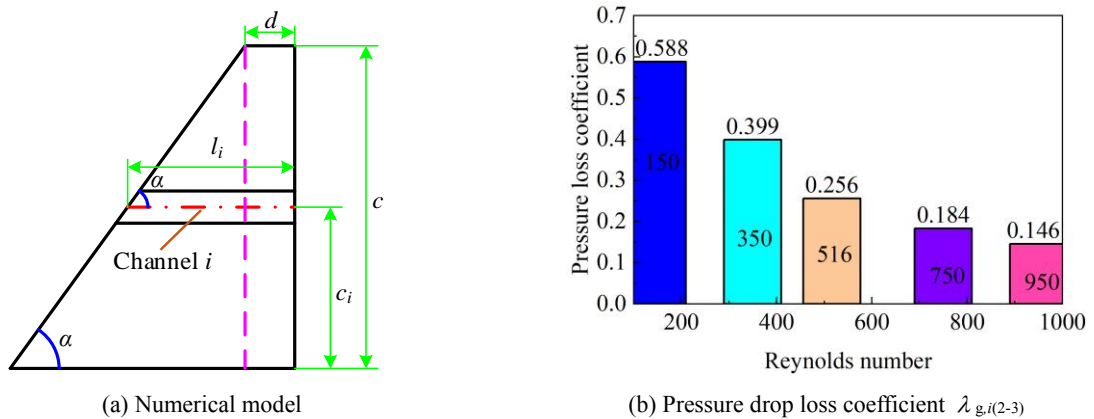


Fig. 13 Pressure drop loss coefficient along channels for gas inlet and outlet structure

3.2.3 Pressure drop losses for 3-4

The gas CW channel has a cross-sectional shape that differs from that of the gas inlet structure channel. A wall exists at the interface 6 between the two channels, as shown in Fig. 14(a). Similar to interface 2 of the air

channel, the local pressure drop loss of the gas channel at interface 6 is modeled as an orifice pressure drop loss. This local pressure drop loss can be expressed by the empirical relationship (3-11). Fig. 15(b) demonstrates that the local pressure loss coefficient $\xi_{g(3-4)}$ at the inlet of gas CW channel increases with the increase of Reynolds number.

$$\Delta p_{g(3-4)} = \xi_{g(3-4)} \frac{\rho_{g(3-4)} \bar{u}_{g4}^2}{2} \quad (3-11)$$

where $\Delta p_{g(3-4)}$, $\rho_{g(3-4)}$, and \bar{u}_{g4}^2 are defined as the pressure drop on both sides of the interface 6, density at gas CW channel inlet, and the average velocity of gas CW channel section, respectively.

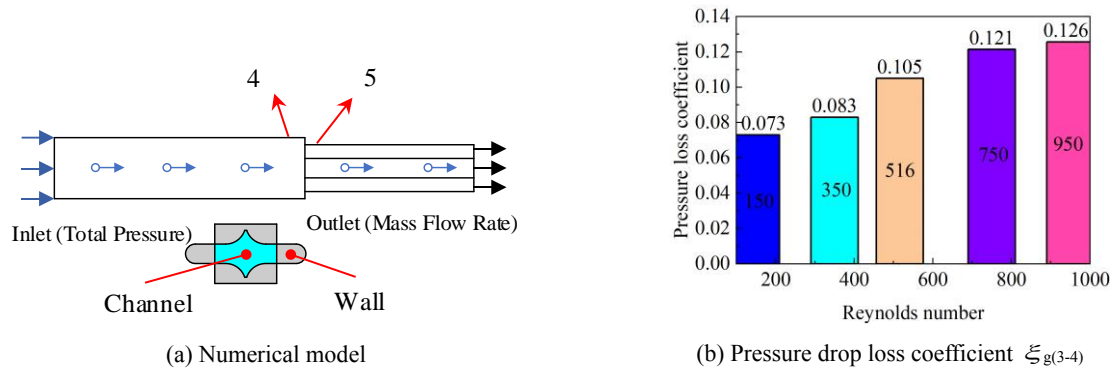


Fig. 14 Local pressure drop loss coefficient at inlet of gas CW channel

3.2.4 Pressure drop losses for 4-5

In Fig. 15(a), the structure of gas CW channel is similar to that of air CW channel. Different from the air CW channel, the airflow direction of the inlet and outlet for the gas CW channel is consistent with the mainstream direction. The pressure drop loss along the gas CW channel is calculated by empirical formula (3-12). In Fig. 15(b), the pressure drop loss coefficient $\lambda_{g,i(4-5)}$ along the gas CW channel first decreases rapidly and then increases slowly with the increase of Reynolds number. The pressure drop loss coefficient reaches its minimum value at a Reynolds number of $Re = 516$.

$$\Delta p_{g,i(4-5)} = \lambda_{g,i(4-5)} \frac{l_{g,cw,i}}{D_{ge,i(4-5)}} \frac{\bar{\rho}_{g(4-5)} \bar{u}_{g(4-5)}^2}{2} \quad (3-12)$$

where $\Delta p_{g,i(4-5)}$, $l_{g,cw,i}$, $D_{ge,i(4-5)}$, $\bar{\rho}_{g,i(4-5)}$, and $\bar{u}_{g,i(4-5)}$ are the pressure drop between inlet and outlet for gas CW channel 4-5, the gas CW channel length, the hydraulic diameter of channel 4-5, the average value of density in the gas CW channel 4-5, and the average value of velocity in the gas CW channel 4-5, respectively.

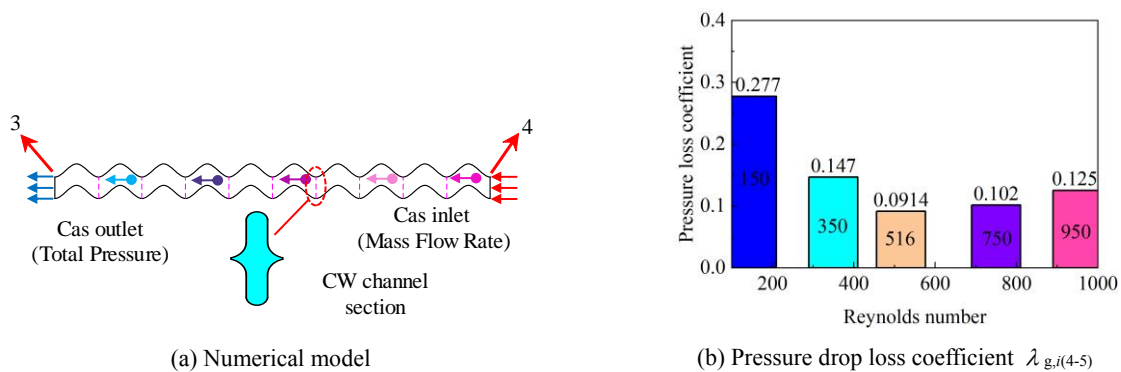


Fig. 15 Pressure drop loss coefficient along gas CW channel

3.2.5 Pressure drop losses for 5-6

Fig. 16(a), demonstrates that the airflow at the outlet of the gas CW channel flows from the CW channel side to the side of the gas inlet structure, with the shape of interface 7 taking the same as interface 6. Therefore, the empirical formula (3-13) of local pressure drop loss at the outlet of gas CW channel is consistent with that at the inlet of gas CW channel. Fig. 16(b) depicts that the local pressure drop loss coefficient $\xi_{g(5-6)}$ at the outlet of gas CW channel fluctuates slightly with Reynolds number, but tends to be constant on the whole.

$$\Delta p_{g(5-6)} = \xi_{g(5-6)} \frac{\rho_{g(5-6)} \bar{u}_{g6}^2}{2} \quad (3-13)$$

where $\Delta p_{g(5-6)}$, $\rho_{g(5-6)}$, and \bar{u}_{g6}^2 are defined as the pressure drop on both sides of the interface 7, the density at the gas CW channel outlet, and the average velocity of channel at the gas outlet structure, respectively.

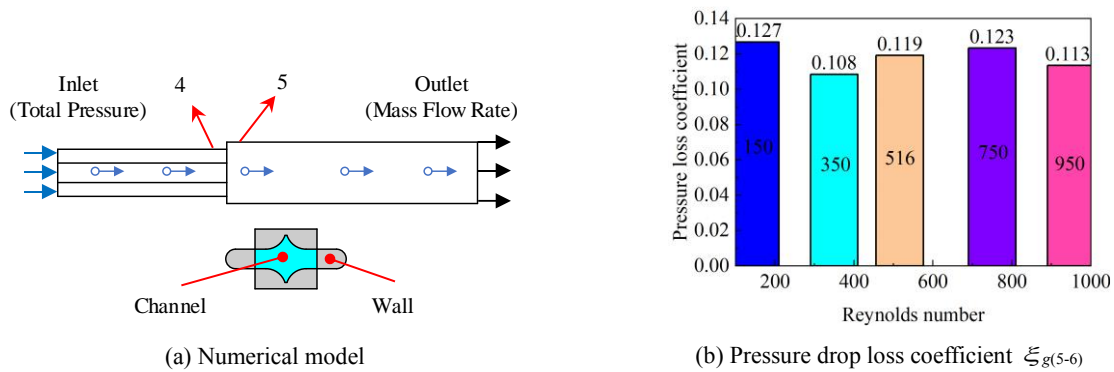


Fig. 16 Local pressure drop loss coefficient at outlet of gas CW channel

3.2.6 Pressure drop losses for 7-8

As shown in Fig. 17(a), the pressure drop loss model at the outlet of the gas channel is a sudden expansion structure. The local pressure drop loss of the sudden expansion structure can be estimated by empirical formula (3-14). As depicted in Fig. 17(b), with the increase of Reynolds number, the pressure drop loss coefficient $\xi_{g(7-8)}$ at the outlet of the gas channel decreases rapidly, and then gradually tends to be constant. Moreover, the local pressure drop loss coefficient at the gas channel outlet is significantly lower than that at the air channel outlet.

$$\Delta p_{g(7-8)} = \xi_{g(7-8)} \frac{\rho_{g(7-8)} \bar{u}_{g8}^2}{2} \quad (3-14)$$

where $\Delta p_{g(7-8)}$, $\rho_{g(7-8)}$, and \bar{u}_{g8}^2 are the pressure drop on both sides of the interface 8, density at the gas channel outlet, and velocity at the section 8, respectively.

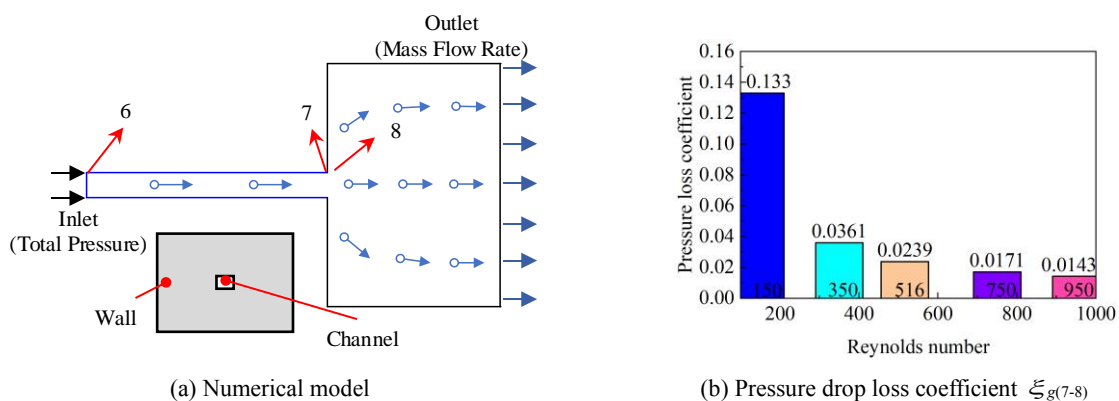


Fig. 17 Local pressure drop loss coefficient at gas channel outlet

3.3 Total pressure drop losses for air and gas side

According to the empirical formula of pressure drop loss of each part, the total pressure drop loss for the air and gas sides can be defined as:

$$\Delta p_{a, \text{Total}} = \Delta p_{a(1-2)} + 2\Delta p_{a,i(2-3)} + \Delta p_{a(3-4)} + \Delta p_{a,i(4-5)} + \Delta p_{a(5-6)} + \Delta p_{a(7-8)} \quad (3-15)$$

$$\Delta p_{g, \text{Total}} = \Delta p_{g(1-2)} + 2\Delta p_{g,i(2-3)} + \Delta p_{g(3-4)} + \Delta p_{g,i(4-5)} + \Delta p_{g(5-6)} + \Delta p_{g(7-8)} \quad (3-16)$$

Therefore, the total relative pressure drop loss for the air and gas sides can be calculated as,

$$\delta p_a = \frac{\Delta p_{a, \text{Total}}}{P_{a, \text{inlet}}} \quad (3-17)$$

$$\delta p_g = \frac{\Delta p_{g, \text{Total}}}{P_{g, \text{inlet}}} \quad (3-18)$$

where $\Delta p_{a, \text{Total}}$ and $\Delta p_{g, \text{Total}}$ are the inlet pressure of the air and gas sides.

4 An application case study

4.1 Geometry and operating parameters

To verify the effectiveness of this pressure drop loss calculation method, we conducted three-dimensional numerical simulations on an annular CWPSR. For the purpose of cost-effective simulation, we selected the heat exchange cell (HEC) of the annular CWPSR as our research object. The geometric parameters of the recuperator are listed in Table 1 and applied to the micro gas turbine with an output power of 7 kW. The temperature and pressure of the air channel inlet are $T_{a, \text{in}}=510.12$ K and $P_{a, \text{out}}=239735$ Pa of the compressor outlet respectively. The inlet temperature and pressure of the gas channel are the outlet temperature $T_{g, \text{in}}=819.17$ k and the outlet pressure $P_{g, \text{out}}=10479$ Pa of the turbine respectively.

Table 1 Geometric parameters of annular CWPSR (mm)

Parameters	<i>a</i>	<i>b</i>	<i>c</i>	<i>d</i>
Value (mm)	12.8	54.5	34.8	0.72

The boundary conditions for the numerical simulation of HEC in the annular CWPSR are presented in Fig. 18 and Table 2. The fluid-solid thermal coupling boundary condition is utilized for the interfaces between the fluid and solid. The mass flow inlet is employed as the boundary condition for the channel inlet of the air and gas. The outlet of the air and gas channels adopt the pressure outlet boundary condition. According to the research of Utriainen [27], the *k-ε* turbulence model with low Reynolds number is more suitable for the numerical simulation of CW channel.

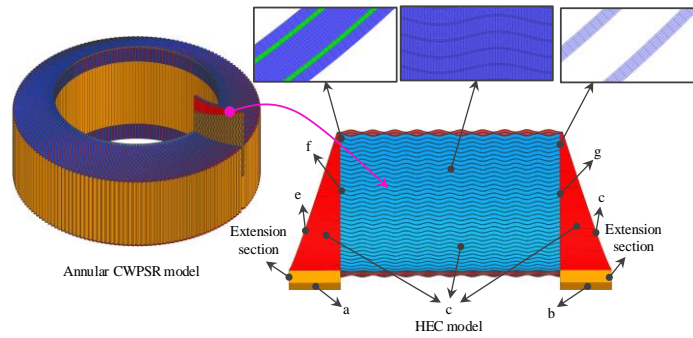


Fig. 18 Numerical model of HEC for annular CWPSR

Table 2 Boundary conditions for numerical simulation of annular CWPSR

Number	a, d	b, e	c	f, g
Boundary condition	Mass flow inlet	Pressure outlet	Symmetry	Interface

To ensure the reliability of the numerical simulation results, it is crucial to verify the independence of HEC grid while maintaining a reasonable grid number. In this study, the fanning friction factor of the air channel is analyzed based on five numerical models with different grid numbers under the same operation conditions. Fig. 19 depicts a gradual increase in the fanning friction factor and Nusselt number Nu of the air channel with the increase in the number of grids. The fanning friction factor of the air channel tends to remain constant when the number of grids reaches 68391711, thus confirming the grid system's suitability for this work.

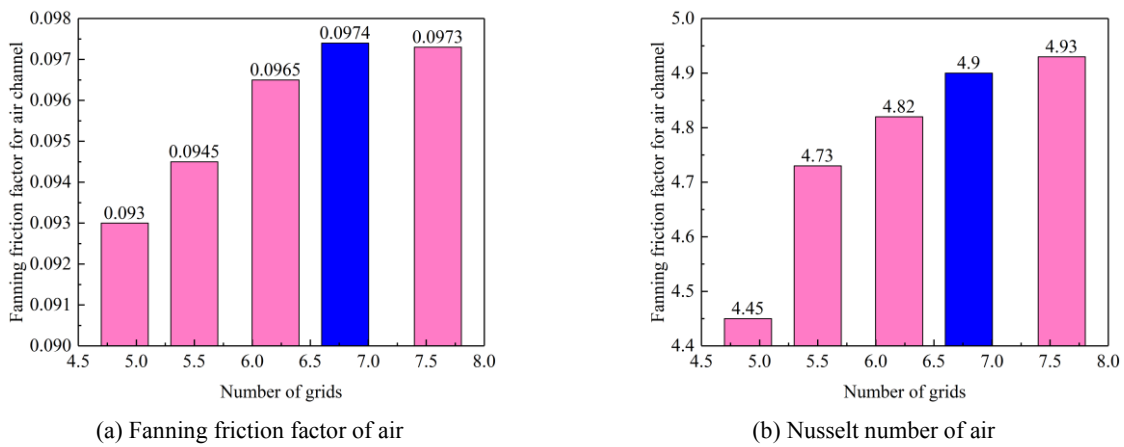


Fig. 19 Grid independence verification for HEC

4.2 Validation of the numerical method

Table 3 summarizes the research results on the flow resistance characteristics of the CW original surface regenerator. Fig. 20 shows a comparison between the fanning friction coefficient obtained from three-dimensional numerical simulation and the empirical data in Table 3. The results indicate good consistency between the numerical results and the data from Utriainen [27] and Ma [34], with maximum relative errors of approximately 9.6% and 10.1%, respectively. However, there is a significant difference with the test results of Liang [30], which can be attributed to the significantly different inlet and outlet structures used in Liang's experiment compared to the HEC used in this study. Additionally, the influence of inlet and outlet structures on flow resistance characteristics is greater than that on heat transfer characteristics. Therefore, the numerical

method employed in this study is credible and acceptable.

Table 3 Correlations of friction factor for annular CWPSR

Researchers	Correlations	Application ranges of Reynolds number
Ma et al. [34]	$f_d=3.182Re-0.398$ ($f_d=4f$)	250<Re<3000
Liang et al. [30]	$f_d=66.63Re-0.64$ ($f_d=4f$)	230<Re<400
Utriainen et al. [27]	$f=0.03131+26.172/Re$ (Type: CW3-z8)	100<Re<950

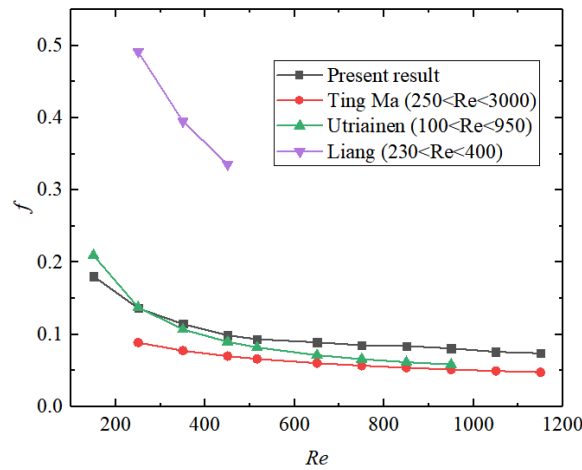


Fig. 20 Comparison of simulation results and experimental data

4.3 Verification of computational method for pressure drop losses

We used three-dimensional numerical simulation technology of HEC to investigate the feasibility of the pressure drop loss calculation method established in this paper with inclination angles of $\alpha=30^\circ$, 45° , and 60° at Reynolds numbers $Re=150$, 350 , 516 , and 750 . The results, as shown in Tables 4, 5, 6, and 7, indicate a good consistency between the total relative pressure drop losses obtained by the computational method established in this work and those calculated by the three-dimensional numerical method for both air and gas channels. For the air channel, the calculation results and numerical simulation data increase gradually with the increase of Reynolds number for $\alpha=30^\circ$, 45° , and 60° . The maximum deviations for $\alpha=30^\circ$, 45° , and 60° are 10.425%, 10.354%, and 10.954%, respectively. Furthermore, the total relative pressure drop loss decreases with the increase of inclination angle α . In the case of the gas channel, the calculation results and numerical simulation data increase gradually with the increase of Reynolds number, and their maximum deviation is 7.151%. In addition, the total relative pressure drop loss on the air side is lower than that on the gas side at Reynolds numbers $Re=150$, 350 , 516 , and 750 .

Table 4 Comparison of total relative pressure drop losses obtained by computational method with numerical simulation results for air channel ($\alpha=30^\circ$)

Reynolds number	150	350	516	750	950
Computational method	0.215%	0.784%	1.674%	3.808%	5.646%
Numerical simulation	0.207%	0.768%	1.600%	3.593%	5.305%
Deviation	6.735%	5.125%	6.598%	8.986%	10.425%

Table 5 Comparison of total relative pressure drop losses obtained by computational method with numerical simulation results for air channel ($\alpha=45^\circ$)

Reynolds number	150	350	516	750	950
Computational method	0.124%	0.701%	1.279%	3.133%	4.576%
Numerical simulation	0.120%	0.680%	1.227%	2.981%	4.303%
Deviation	6.241%	6.124%	7.265%	8.114%	10.354%

Table 6 Comparison of total relative pressure drop losses obtained by computational method with numerical simulation results for air channel ($\alpha=60^\circ$)

Reynolds number	150	350	516	750	950
Computational method	0.183%	0.805%	1.251%	2.860%	4.214%
Numerical simulation	0.178%	0.787%	1.210%	2.727%	3.977%
Deviation	5.635%	5.341%	6.356%	8.866%	10.954%

Table 7 Comparison of total relative pressure drop losses obtained by computational method with numerical simulation results for gas channel

Reynolds number	150	350	516	750	950
Computational method	0.497%	1.898%	3.146%	6.852%	12.159%
Numerical simulation	0.476%	1.814%	2.993%	6.450%	11.348%
Deviation	4.351%	4.652%	5.124%	6.235%	7.151%

5 Conclusions:

Achieving a low pressure drop loss is crucial for the annular CWPSR in the micro gas turbine. One of the key factors that affects the pressure drop loss of the annular CWPSR is the inclination angle α of the inlet structure. Therefore, it is necessary to study the calculation method of pressure drop loss for this system. In this study, we divided the air channel and gas channel of HEC for the annular CWPSR into six parts based on the type of pressure drop loss. We then established a mathematical model based on the pressure drop loss type for each part, and calculated each pressure drop loss coefficient using three-dimensional numerical simulation one by one. To investigate the impact of the inclination angle α of the inlet structure on the pressure drop loss of the annular CWPSR, we selected physical models with $\alpha=30^\circ$, 45° , and 60° as the research objects. Finally, we used the fluid-solid heat coupling numerical model of HEC validated by test data to verify the reliability of the pressure drop loss model of the annular CWPSR. Our computational method showed good consistency with the three-dimensional numerical method for both the air channel and gas channel. For the air channel, the maximum deviations between calculation results and numerical simulation data corresponding to $\alpha=30^\circ$, 45° , and 60° were 10.425%, 10.354%, and 10.954%, respectively. For the gas channel, the maximum deviation was 7.151%. Additionally, the total relative pressure drop loss on the air side was lower than that on the gas side at Reynolds numbers $Re=150$, 350, 516, and 750.

Acknowledgement

This research is supported by the National Natural Science Foundation of China (Grant No. 52006045). We would like to thank all those who reviewed and contributed to this paper for their valuable assistance.

References:

- [1] Pornet C, Isikveren A T. “Conceptual Design of Hybrid-Electric Transport Aircraft,” *Progress in Aerospace Sciences*, 2015, 79: 114-135. Doi: 10.1016/j.paerosci.2015.09.002.
- [2] Schäfer A W, Evans A D, Reynolds T G, et al. “Costs of Mitigating CO2 Emissions from Passenger Aircraft,” *Nature Climate Change*, 2016, 6(4): 412-417.. Doi: 10.1038/nclimate2865.
- [3] Gnadt A R, Speth R L, Sabnis J S, et al. “Technical and Environmental Assessment of All-Electric 180-passenger Commercial Aircraft,” *Progress in Aerospace Sciences*, 2019, 105: 1-30. Doi: 10.1016/j.paerosci.2018.11.002.
- [4] Barzkar A, Ghassemi M. “Electric Power Systems in More and All Electric Aircraft: A Review,” *IEEE Access*, 2020. Doi: 10.1109/ACCESS.2020.3024168.
- [5] Schäfer A W, Barrett S R H, Doyme K, et al. “Technological, Economic and Environmental Prospects of All-Electric Aircraft,” *Nature Energy*, 2019, 4(2): 160-166. Doi: 10.1038/s41560-018-0294-x.
- [6] Kakaras L F D P. “Integrated CHP with autothermal biomass gasification and SOFC–MGT,” *Energy Conversion and Management*, 2008: DOI:10.1016/j.enconman.2007.06.013.
- [7] Duan L , He B , Yang Y. “Parameter optimization study on SOFC - MGT hybrid power system,” *International Journal of Energy Research*, 2011, 35(8):721-732. DOI:10.1002/er.1725.
- [8] Tola C V. “SOFC-MGT hybrid power plants fuelled by methanol and DME,” *Journal of Applied Electrochemistry*, 2008. DOI:10.1007/s10800-008-9508-4.
- [9] Perna A , Minutillo M , Jannelli E ,et al. “Performance assessment of a hybrid SOFC/MGT cogeneration power plant fed by syngas from a biomass down-draft gasifier,” *Applied Energy*, 2017:80-91. DOI: 10.1016/j.apenergy.2017.08.077.
- [10] Kawabata Y , Tachikawa Y , Taniguchi S ,et al. “New Applications of SOFC-MGT Hybrid Power Generation System for Low-Carbon Society,” *ECS Transactions*, 2017, 78(1):197-208. DOI: 10.1149/07801.0197ecst.
- [11] R Dückerhoff, Berg H P , Himmelberg A ,et al. “Influence on the Electrical Efficiency of a Hybrid MGT-SOFC-System by μ -fogging in a-Two-Stage Compressor System,” *IOP Conference Series: Materials Science and Engineering*, 2020, 886(1): 012041 (8pp). DOI: 10.1088/1757-899X/886/1/012041.
- [12] Berg H P , Kleissl M , Himmelberg A ,et al. “Heat balancing of direct reforming fuel cells in MGT-SOFC hybrid systems,” *IOP Conference Series Materials Science and Engineering*, 2019, 501(1): 012007. DOI: 10.1088/1757-899X/501/1/012007.
- [13] Di,Carlo,Borello,et al. “Process simulation of a hybrid SOFC/mGT and enriched air/steam fluidized bed gasifier power plant,” *INT J HYDROGEN ENERG*, 2013, 2013,38(14)(-):5857-5874. DOI: 10.1016/j.ijhydene.2013.03.005.
- [14] Andrea,Di,Carlo,et al. “Process simulation of a hybrid SOFC/mGT and enriched air/steam fluidized bed gasifier power plant,” *International Journal of Hydrogen Energy*, 2013. DOI: 10.1016/j.ijhydene.2013.03.005.
- [15] Waters D F, Cadou C P. “Engine-Integrated Solid Oxide Fuel Cells for Efficient Electrical Power Generation on Aircraft,” *Journal of Power Sources*, 2015, 284:588-605. Doi: 10.1016/j.jpowsour.2015.02.108.
- [16] Ji Z, Qin J, Cheng K, et al. “Thermodynamic Analysis of a Solid Oxide Fuel Cell Jet Hybrid Engine for Long-Endurance Unmanned Air Vehicles,” *Energy Conversion and Management*, 2019, 183:50-64. Doi: 10.1016/j.enconman.2018.12.076.
- [17] Cocco D , Tola V. “Use of alternative hydrogen energy carriers in SOFC-MGT hybrid power plants,” *Energy Conversion & Management*, 2009, 50(4):1040-1048. DOI:10.1016/j.enconman.2008.12.019.
- [18] Savino S , Comini G , Nonino C. “Effect of corner angle on convection enhancement in wavy ducts with trapezoidal cross-sections,” *International Journal for Numerical Methods in Fluids*, 2004, 44. DOI: 10.1002/fld.686.
- [19] Yau H T , Wang C C , Cho C C ,et al. “A NUMERICAL INVESTIGATION INTO ELECTROSMOTIC FLOW IN MICROCHANNELS WITH COMPLEX WAVY SURFACES,” *Thermal Science*, 2011, 15(suppl.1): 87-94. DOI: 10.2298/

TSCI11S1087Y.

- [20] Sucipta M , Kimijima S , Suzuki K. “Performance analysis of the SOFC–MGT hybrid system with gasified biomass fuel,” *Journal of Power Sources*, 2007, 174(1):124-135. DOI:10.1016/j.jpowsour.2007.08.102.
- [21] You H , Han J , Liu Y ,et al. “4E analysis and multi-objective optimization of a micro poly-generation system based on SOFC/MGT/MED and organic steam ejector refrigerator,” *Energy*, 2020, 206. DOI: 10.1016/j.energy.2020.118122.
- [22] Krummrein T , Henke M , Kutne P ,et al. “Corrigendum to 'Numerical analysis of operating range and SOFC-off-gas combustor requirements of a biogas powered SOFC-MGT hybrid power plant' [Appl. Energy 232 (2018) 598-606],” *Applied Energy*, 2019, 235(FEB.1):1668-1668. DOI: 10.1016/j.apenergy.2018.10.079.
- [23] Krummrein T , Henke M , Kutne P ,et al. “Numerical analysis of operating range and SOFC-off-gas combustor requirements of a biogas powered SOFC-MGT hybrid power plant,” *Applied Energy*, 2018, 232:598-606. DOI: 10.1016/j.apenergy.2018.09.166.
- [24] Capstone Turbine Coporation, “Advanced MicroTurbine system (AMTS): C200 micro turbine and ultra-low emissions MicroTurbine,” United States, March 31, 2007. Doi:10.2172/975026.
- [25] G. Lagerstrm, and M. Xie, “High Performance and Cost Effective Recuperator for Micro-Gas Turbines,” *ASME Turbo Expo*, 2002: Power for Land, Sea, and Air, pp. 1003-1007, June 3–6, 2002. Doi: 10.1115/GT2002-30402.
- [26] E. Utriainen and B. Sundén. "Recuperators in Gas Turbine Systems." *Proceedings of the ASME 1998 International Gas Turbine and Aeroengine Congress and Exhibition*. Vol. 3, June 2–5, 1998. Doi: 10.1115/98-GT-165.
- [27] E. Utriainen, and B. Sundén, “Numerical analysis of a primary surface trapezoidal cross wavy duct,” *International Journal of Numerical Methods for Heat & Fluid Flow*, Vol. 10, No. 6 pp. 634-648, September 1, 2000. Doi: doi.org/10.1108/09615530010347213.
- [28] E. Utriainen, and B. Sundén, “A Comparison of Some Heat Transfer Surfaces for Small Gas Turbine Recuperators,” *Asme Turbo Expo: Power for Land, Sea, & Air*, Vol. 3, June 4–7, 2001. Doi: 10.1115/2001-GT-0474.
- [29] Q. W. Wang, et al., “Experimental investigation on heat transfer and pressure drop in a microturbine recuperator with cross-wavy primary surface channels,” In: *ASME turbo expo*, Vol. 3, pp.293-298, June 6–9, 2005. Doi: 10.1115/GT2005-68255.
- [30] H. X. Liang, Q. W. Wang, and J. W. Wang, “Experimental study on flow and heat transfer of CW primary surface recuperator for microturbine,” *J Eng Thermophys*, Vol. 27, pp. 865-7, September 1, 2006.
- [31] L. X. Du, T. Ma, M. Zeng, Z. X. Guo and Q. W. Wang, “Numerical Investigations on the Thermohydraulic Performance of Cross-Wavy Channels with Multi-Periodic Boundary Conditions,” *Numerical Heat Transfer, Part A: Applications*, Vol. 65, pp.732-749, 2014. DOI: 10.1080/10407782.2013.846634.
- [32] J. W. Seo, C. Y. Cho, S. Lee, and Y. D. Choi, “Thermal Characteristics of a Primary Surface Heat Exchanger with Corrugated Channels,” *Entropy*, Vol. 18, pp.15, 2016. DOI: 10.3390/e18010015.
- [33] T. Ma, et al., “Experimental and numerical study on heat transfer and pressure drop performance of Cross-Wavy primary surface channel,” *Energy Conversion & Management, Entropy*, Vol. 125, pp.80-90, 2016. DOI: 10.1016/j.enconman.2016.06.055.
- [34] Yue-Tzu Yang, Hsiang-Wen Tang and Shih-Jie Jian, “Numerical simulation and optimization of turbulent nanofluids in a three-dimensional wavy channel,” *Numerical Heat Transfer, Part A: Applications*, Vol. 69, pp.1169-1185, 2016. DOI: 10.1080/10407782.2015.1125729.
- [35] J. Cai, X. Huai, and W. Xi, “An optimal design approach for the annular involute-profile cross wavy primary surface recuperator in microturbine and an application case study,” *Energy*, Vol. 153, pp.80-89, 2018. DOI: 10.1016/j.energy.2018.04.016.
- [36] X. S. Shi, Y. W. Wang, X. L. Huai, and K. Cheng, “Influence of structure parameters on entropy generation performance in cross wavy channels with fluid-solid coupled heat transfer,” *Applied Thermal Engineering*, Vol. 181, pp. 115882, 2020. DOI:

10.1016/j.applthermaleng.2020.115882.

- [37] H Li, et al., “Thermal performance of a microchannel primary surface recuperator for portable microturbine generators: Design and experimental study,” *Applied Thermal Engineering*, Vol. 206, pp. 118103, 2022. DOI: 10.1016/j.applthermaleng.2022.118103.
- [38] H. G. Kwon, D. H. Sang, and H. H. Cho, “Flow and heat/mass transfer in a wavy duct with various corrugation angles in two dimensional flow regimes,” *Heat & Mass Transfer*, Vol. 45, pp. 157–165, 2008. DOI: 10.1007/s00231-008-0422-4.